




ORIGINAL RESEARCH ARTICLE

Magnetic and DC Electrical Properties of Cu Doped Co–Zn Nanoferrites

P. HIMAKAR,¹ N. MURALI ,^{2,7} D. PARAJULI,¹ V. VEERAIHAH,¹
K. SAMATHA,¹ TULU WEGAYEHU MAMMO,³
KHALID MUJASAM BATOO,^{4,8} MUHAMMAD HADI,⁵ EMAD H. RASLAN,⁵
and SYED FAROOQ ADIL⁶

1.—Department of Physics, Andhra University, Visakhapatnam, Andhra Pradesh, India. 2.—Department of Engineering Physics, AUCE (A), Andhra University, Visakhapatnam, India. 3.—Department of Physics, CNCS, Aksum University, Axum, Ethiopia. 4.—King Abdullah Institute for Nanotechnology, King Saud University, P.O. Box-2455, Riyadh 11451, Saudi Arabia. 5.—Department of Physics, College of Science, King Saud University, P.O. Box-2455, Riyadh 11451, Saudi Arabia. 6.—Department of Chemistry, College of Science, King Saud University, P.O. Box-2455, Riyadh 11451, Saudi Arabia. 7.—e-mail: muraliphdau@gmail.com. 8.—e-mail: kbatoo@ksu.edu.sa

Cu-doped Co–Zn nanoferrites $\text{Co}_{0.5}\text{Cu}_x\text{Zn}_{0.5-x}\text{Fe}_2\text{O}_4$ ($x = 0.0, 0.2$ and 0.4) were synthesized by sol-gel auto-combustion. X-ray diffraction (XRD), field emission scanning electron microscopy (FESEM) with EDS, Fourier transform infrared (FTIR) spectroscopy, vibrating sample magnetometry (VSM), and two-probe methods were employed to study the structural, morphological, magnetic and DC electrical resistivity properties, respectively, of the prepared samples. Monotonically decreasing values of the lattice constants with the dopant concentrations were calculated. The crystallite sizes were also recorded in a decreasing pattern. The stretching bond vibrations measured by room temperature FT-IR showed characteristic absorptions in the range of $579.634\text{--}393.49\text{ cm}^{-1}$. The magnetic parameters were observed to have a tuned value, although decreasing in a non-monotonic pattern. A higher value of the DC resistivity value was recorded for $x = 0.2$ concentration of the dopant, indicating the optimal concentration for synthesizing materials applicable in high-frequency microwave devices.

Key words: Co–Zn–Cu ferrite spinel, XRD, FESEM, FTIR, VSM

INTRODUCTION

Due to the unusual electric and magnetic behavior of nanoferrites and their composites, these materials are under extensive study.^{1–3} Ferrites are useful in magnetic recording devices, wave absorbers and microwave device applications.^{4,5} Ferrite nanoparticles of the type AB_2O_4 have a spinel structure with A^{2+} divalent and B^{3+} trivalent atoms in tetrahedral and octahedral sites.⁶ Cobalt

ferrite CoFe_2O_4 is one of the hard ferrites, having a spinel structure with partial inversion. The octahedral site A is dominated by Co^{2+} ions and the tetrahedral site by Fe^{3+} ions.⁷ These sites with Fe^{3+} and Co^{2+} ions have magnetic moments of $5\mu_B$ and $3\mu_B$, respectively.^{8,9} The cation distribution in different sites is of utmost importance with regard to how a spinel structure behaves. Transformation of total cation from A to B and half transformation from B to A results in an inverted spinel. The cation proportion change will alter the resulting material's properties.^{10–12} Substituting zinc in a limited proportion in cobalt ferrite can produce positive changes in spinel structure properties, such as

(Received August 27, 2020; accepted January 18, 2021; published online March 5, 2021)

magnetic properties and electrical resistivity, sufficient for sensor and actuator applications.^{13,14} Researchers' approaches for preparing these nanoferrites include microemulsion, co-precipitation, ceramic, hydrothermal and various sol-gel techniques.^{15–18} In this research, we chose to use sol-gel auto combustion to synthesize Cu substituted Co-Zn ferrite nanoparticles. The process is clean and offers reasonable stoichiometric control. It produces ultrafine particles in a short processing time at low temperature.¹⁹

In the present paper, we report the synthesis procedures of $\text{Co}_{0.5}\text{Cu}_{0.2}\text{Zn}_{0.5-x}\text{Fe}_2\text{O}_4$ ($x = 0.0, 0.2$ and 0.4) nanoferrites using sol-gel auto-combustion. Efforts have been made to identify the influence of Cu doping on the structural, magnetic, and DC electrical resistivity properties of $\text{Co}_{0.5}\text{Zn}_{0.5}\text{Fe}_2\text{O}_4$. Various characterization techniques were employed, such as x-ray powder diffraction (XRD), field emission scanning electron microscopy (FESEM) with energy dispersive spectroscopy (EDS), Fourier transform infrared (FTIR) spectroscopy, vibrating sample magnetometer (VSM), and electrical resistivity measurements by two-probe methods. To the best of our knowledge, no information is available in the literature about the magnetic properties of $\text{Co}_{0.5}\text{Cu}_{0.2}\text{Zn}_{0.5-x}\text{Fe}_2\text{O}_4$ nanoferrites for compositions $x = 0.2$ and 0.4 synthesized by sol-gel auto-combustion.

EXPERIMENTAL PROCEDURES

AR grade metal nitrates with 99% purity of cobalt, zinc, copper nitrates and citric acid mixed in 1:1 M ratio were used as the precursors. Citric acid helps in the formation of the colloidal solution of the product. The interaction between oxygen and metal ions while stirring, heating and dehydrating the sample controls the nitrates' precipitation. As a result, a single phased ferrite material was prepared at low synthesis temperature. The addition of ammonia kept the solution neutral. The product was mixed with water for a more transparent solution. The solution was continuously heated up to 150°C upon stirring until it became a gel. Combustion of the gel converted it into ash. The ash was ground into fine powdered particles and sintered at 1050°C for 3 hrs to arrive at the intended result. To a powder sample ground with PVA, a pressure of 5 tons was applied so that disc-shaped pellets were formed. These pellets were used for electrical characterization.

Rigaku Miniflex II XRD incorporating the $\text{CuK}\alpha$ radiation of 1.5406 \AA wavelength and TESCAN, MIRA II LMH SEM was used for structural and the morphological texture analysis. The EDS, Inca Oxford, along with the FESEM, gives the elemental composition and FT-IR provides information about functional groups. The EZ VSM model was employed at room temperature to study magnetic

properties. The DC resistivities were measured with the help of a two-probe DC resistivity technique.

RESULTS AND DISCUSSION

XRD Analysis

To detect a spinel structure with a single-phase, $\text{CuK}\alpha$ ($\lambda=1.5406 \text{ \AA}$) radiation of XRD was used for scanning the synthesized samples $\text{Co}_{0.5}\text{Cu}_x\text{Zn}_{0.5-x}\text{Fe}_2\text{O}_4$ ($x = 0.0, 0.2$ and 0.4) at different angles, in the Bragg angle (2θ) range of 10° to 80° . The x-ray diffraction analysis revealed the phase formation of the anticipated spinel ferrite material with a single-phase and Fd-3m crystal symmetry. A similar result has been reported by Singh et al.⁶ for $\text{Co}_x\text{Zn}_{1-x}\text{Fe}_2\text{O}_4$ ($0 \leq x \leq 1$) nanoferrites. The smooth and sharp peaks in the XRD pattern indicate the well-crystallized and pure spinel nature of single-phase ferrite nanoparticles. The diffraction lines of the respective planes, as revealed by Fig. 1, were matched for comparison with the standard indexed data of the materials and found to match ICCD # 00-008-0234.²⁰

For a known value of d (interplanar spacing) and the planes' (hkl) values, using Bragg's diffraction law, the lattice parameter value was calculated as,²¹

$$a = d_{\text{hkl}} \sqrt{h^2 + k^2 + l^2}.$$

The variation of ' a ' with Cu concentration in $\text{Co}_{0.5}\text{Cu}_x\text{Zn}_{0.5-x}\text{Fe}_2\text{O}_4$ ($x = 0.0, 0.2$, and 0.4) samples is shown in Fig. 2. As shown in the figure, the lattice parameter decreases with the dopant's concentration, with a maximum value of 8.4214 \AA with $\pm 0.002 \text{ \AA}$ accuracy for the parent material. These

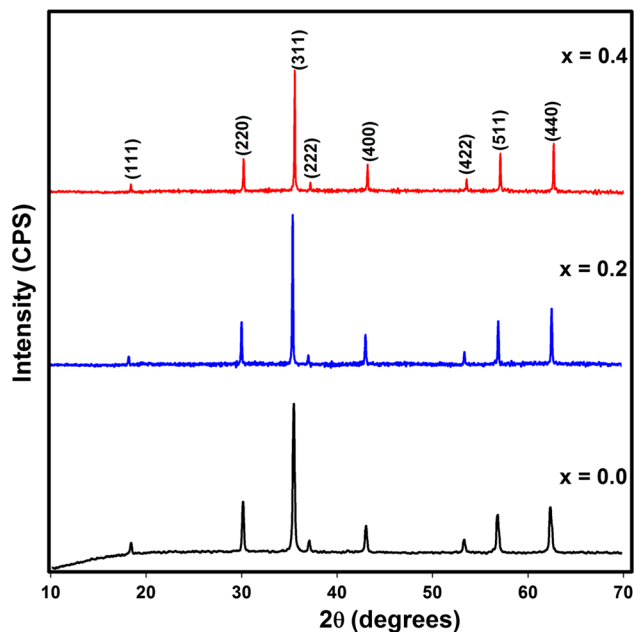


Fig. 1. XRD patterns of $\text{Co}_{0.5}\text{Cu}_x\text{Zn}_{0.5-x}\text{Fe}_2\text{O}_4$ nanoferrites.

results agree with our previous reports and other researchers' reports; and lower values of the crystallite sizes have been obtained.^{22,23} Thus, the prepared materials are in the nanoscale range, which could exhibit nanoparticle behaviors applicable in different technological outputs. Table I displays all such values. The decrease in the value of the lattice constant is due to the substitution of the larger ionic radius cation Zn^{2+} (0.74 Å) by the smaller ionic radius Cu^{2+} (0.71 Å) ions.^{24,25}

Scherer's formula²⁶ below relates the magnitude of peak broadening and all samples' crystallite sizes.

$$D_{311} = \frac{0.9\lambda}{\beta \cos \theta},$$

where D_{311} denotes the crystallite size, λ represents the x-ray wavelength utilized, β is the full width at half maximum (FWHM) of (311) peak and θ is the angle of diffraction. β is the corrected value in radians. Figure 2 shows that the crystallite size first decreased and then increased with Cu^{2+} concentration, as in Table I. Similar behavior was also reported for Nd^{3+} -substituted Co–Zn nanoferrites by Almessiere.²⁷

FESEM and EDS Analysis

The three-dimensional FESEM images show the grain and porosity structures, as depicted in Fig. 3. These microstructures significantly determine the properties of the synthesized samples. The

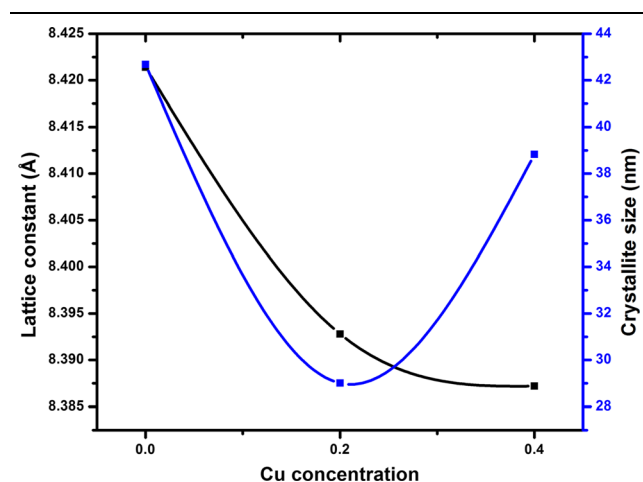


Fig. 2. Variation of lattice constant and crystallite size of $\text{Co}_{0.5}\text{Cu}_x\text{Zn}_{0.5-x}\text{Fe}_2\text{O}_4$ nanoferrites.

figure reveals grains of irregularly shaped and various sizes. It seems grains of smaller size coalesced together to develop relatively larger grains as the Cu^{2+} was being doped. Although the surface texture for the sample with $x = 0.2$ concentration of Cu^{2+} looks fine-grained, bigger grains can be observed underlying these refined grains. A slight change in the porosity level can be observed from the images with a non-uniform distribution. Obviously, in ceramic materials, inter-granular porosity decreases with expanding grain size.²⁸ The fine-grained microstructures of Co–Zn–Cu mixed ferrites obtained by a sol-gel synthesis method were reported by Mane et al.²⁹ The results of that study seem similar to the results of this present report with regard to the pattern of these microstructure developments.

The images show clear grains in an almost non-agglomerated state, which helps our grain size calculator identify the grain boundaries; we used Image J software to measure the grain size. The average grain sizes were found to be around 81, 74, and 78 nm for $\text{Co}_{0.5}\text{Cu}_x\text{Zn}_{0.5-x}\text{Fe}_2\text{O}_4$ nanoferrites with $x = 0.0, 0.2, 0.4$, respectively. The obtained results show behavior similar to the crystallite sizes calculated using XRD patterns. Such grain sizes confirm the nanoscale level of the synthesized sample in agreement with the XRD results. Such grain sizes are supposed to significantly influence the magnetic properties, even though many other parameters, such as the substituent cations' magnetic moment, also influence magnetic properties.

EDS is used for the compositional analysis of the ferrites. The EDS spectrum for each sample is shown in Fig. 4. The figures indicate the existence of Co, Cu, Zn, Fe, and O. Table II and the histogram in Fig. 5 give the weight and atomic percentages of the ferrite calculated using EDS. Moreover, the EDS indicates roughly the stoichiometric compositions of the as-synthesized samples.

FTIR Analysis

The sintered powders of $\text{Co}_{0.5}\text{Cu}_x\text{Zn}_{0.5-x}\text{Fe}_2\text{O}_4$ ($x = 0.0, 0.2$ and 0.4) were investigated using FT-IR spectra in the wavenumber ranging between 350–1200 cm^{-1} , as Fig. 6 displays. Here, the incident radiation having the appropriate wavenumber vibrates the metal ions, indicating the material's special and unique property. The cubic spinel structure has two such bands due to their two types of ions residing in two different positions:

Table I. Lattice constants and crystallite size of $\text{Co}_{0.5}\text{Cu}_x\text{Zn}_{0.5-x}\text{Fe}_2\text{O}_4$ nanoferrites

Composition (x)	Lattice constant (Å)	Crystallite size (nm)	Space group
0.0	8.4214	42.68	<i>Fd-3m</i>
0.2	8.3928	29.01	<i>Fd-3m</i>
0.4	8.3872	38.83	<i>Fd-3m</i>

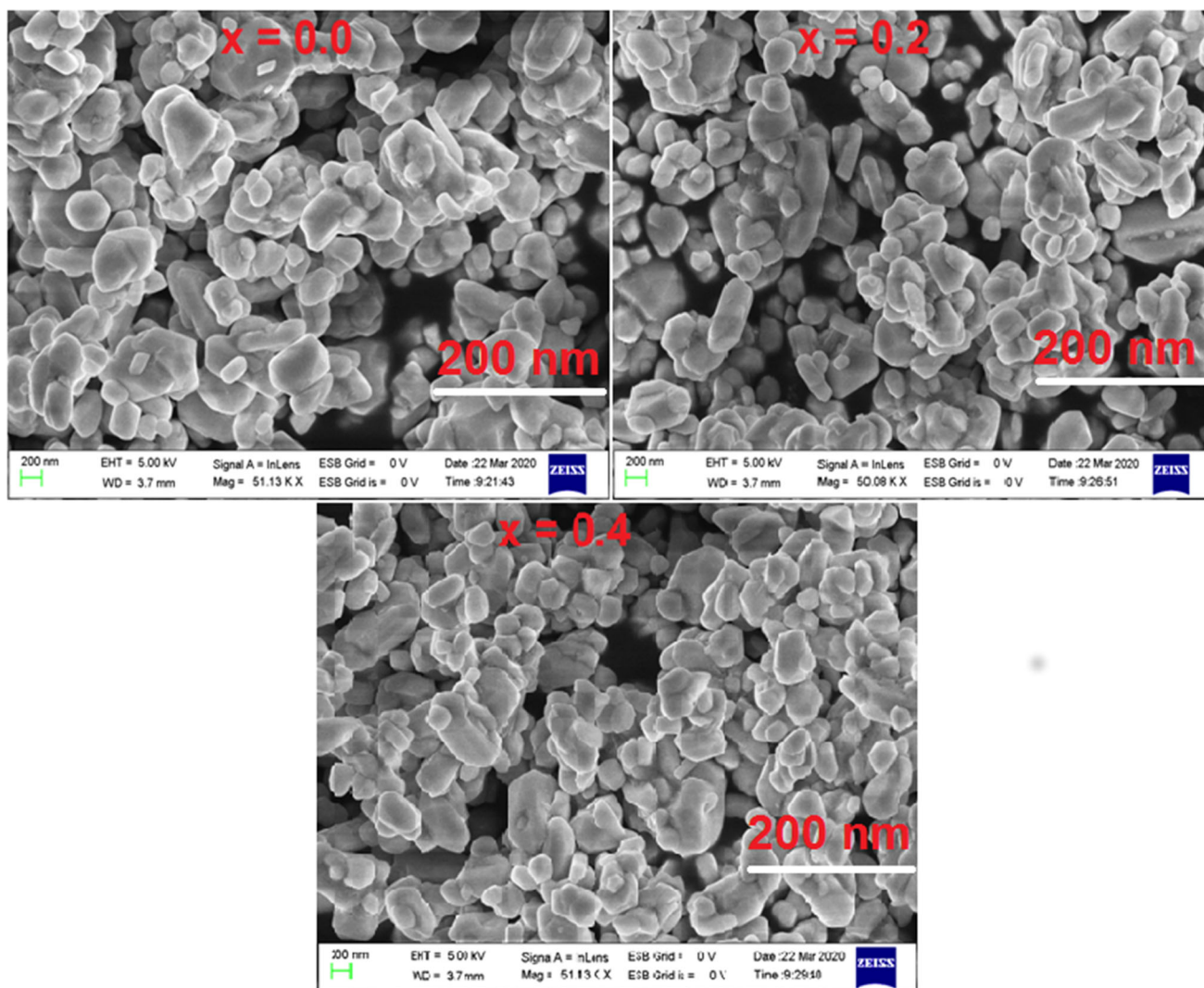


Fig. 3. FESEM images for $\text{Co}_{0.5}\text{Cu}_x\text{Zn}_{0.5-x}\text{Fe}_2\text{O}_4$ nanoferrites.

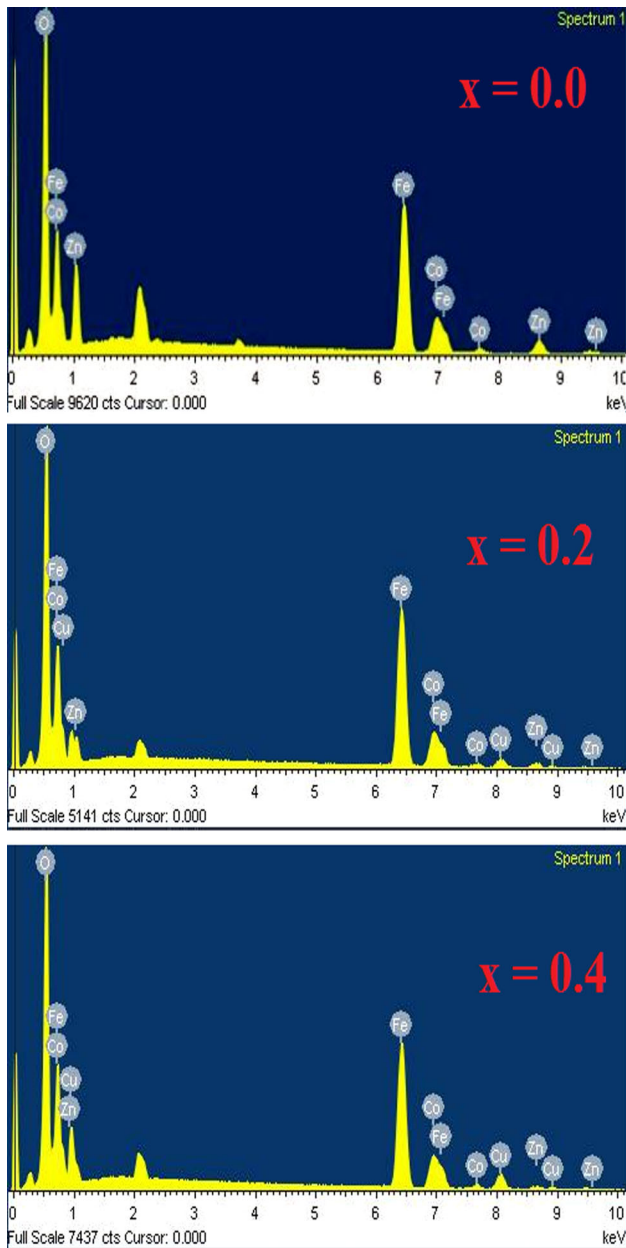
tetrahedral denoted as A and octahedral as B.³⁰ The higher frequency band (say, ν_1) corresponds to the vibrational stretching on the tetrahedral position, and the lower frequency band (say, ν_2) corresponds to that on the octahedral position.^{31,32} The tetrahedral and octahedral bands lie in the ranges of $524.661\text{--}579.634\text{ cm}^{-1}$ and $399.28\text{--}393.49\text{ cm}^{-1}$, respectively, as listed in Table III. The usual range of vibration for a spinel structure is from $400\text{--}600\text{ cm}^{-1}$. Here, the octahedral vibrational band is lower than this range.

We know that the vibrational frequency (wavenumber) depends upon the mass of the cation, the bonding force and distance between the cation and oxygen, and unit cell parameters. Further, the distance between cation (Fe^{3+}) and anion (O^{2-}) has a major role, and was found to be 1.89 \AA for A site and 1.99 \AA for B site. Since the ionic radius of Cu^{2+} (0.73 \AA) is less than that of Fe^{2+} (0.75 \AA) and Zn (0.88 \AA), the site radius decreases. Incrementing Cu^{2+} concentration decreases the site radius, which

reduces the unit cell dimension and hence decreases the wavenumber (increases the fundamental frequency). This is why the absorption band on the octahedral site shifted towards the lower wavenumber side, i.e. below 400 cm^{-1} . Overall, the characteristic band absorptions at the octahedral and tetrahedral reveal the synthesized materials' structured spinel nanoparticles.

VSM Study

The vibrating sample magnetometer (VSM) was used to study the magnetic properties of the $\text{Co}_{0.5}\text{Cu}_x\text{Zn}_{0.5-x}\text{Fe}_2\text{O}_4$ ($x = 0.0, 0.2$ and 0.4) nanoferrite materials. The hysteresis loops for respective concentrations obtained from VSM under the field of $\pm 10,000\text{ Oe}$ are shown in Fig. 7. The S-shaped hysteresis loop indicates that the sample is the ferrimagnetic, and higher coercive value of these samples reveals that these materials are hard ferrimagnetic ferrites.^{33,34} The higher the retentivity values (the lower the coercivity), the more easily

Fig. 4. EDS counts for $\text{Co}_{0.5}\text{Cu}_x\text{Zn}_{0.5-x}\text{Fe}_2\text{O}_4$ nanoferrites.

these materials can be magnetized and the more rapidly they can be demagnetized. The value of saturation magnetization (M_s) decreases quickly with Cu doping and increased Cu concentration, as shown in Fig. 8. The exchange interaction between the ions at tetrahedral and octahedral sites may cause this effect. The particle and magnetic domain size-reduction decreases the coercivity and hence H_c .³⁵⁻³⁷ A semi-disordered system like Co-Zn ferrite, exhibiting a sudden tilting or over-turning effect (canting) in magnetic moments, decreases the magnetization.³⁸ Ferrites having high M_s and moderate H_c ³⁹ are required for magnetic recording media applications.⁴⁰

M_A and M_B represent the magnetic moments at the tetrahedral and octahedral sites; the difference in these magnetic moments at the two sites gives net magnetic moment $M_s = |M_B - M_A|$. Moreover, Fig. 8 shows the coercivity increased with the concentration of Cu and then decreased. Here, the sample at $x = 0.2$ has more coercivity. The calculated saturation magnetization (M_s), remnant magnetization (M_r), coercive field (H_c), and theoretical

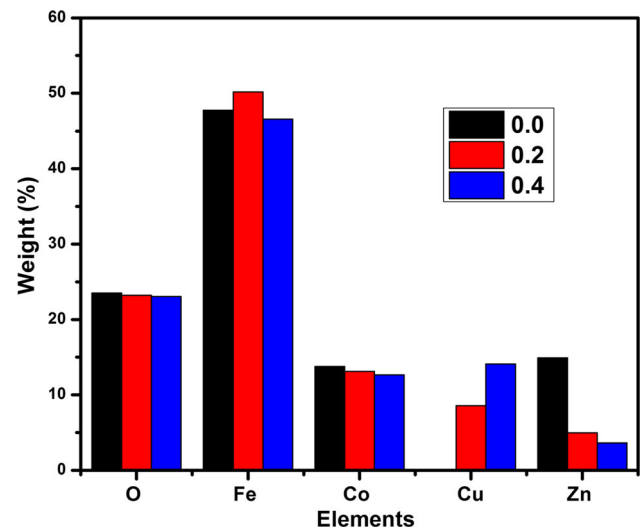
Fig. 5. Histogram of $\text{Co}_{0.5}\text{Cu}_x\text{Zn}_{0.5-x}\text{Fe}_2\text{O}_4$ nanoferrites.

Table II. Composition by (weight%), (atomic%) of each sample using EDS

Composition	$x = 0.0$		$x = 0.2$		$x = 0.4$	
	Weight %	Atomic %	Weight %	Atomic %	Weight %	Atomic %
O	23.52	52.74	23.22	52.16	23.06	52.09
Fe	47.78	30.69	50.15	32.27	46.58	30.14
Co	13.78	8.39	13.12	8.00	12.65	7.76
Cu	—	—	8.55	4.84	14.08	6.01
Zn	14.92	8.18	4.97	2.73	3.62	2.00

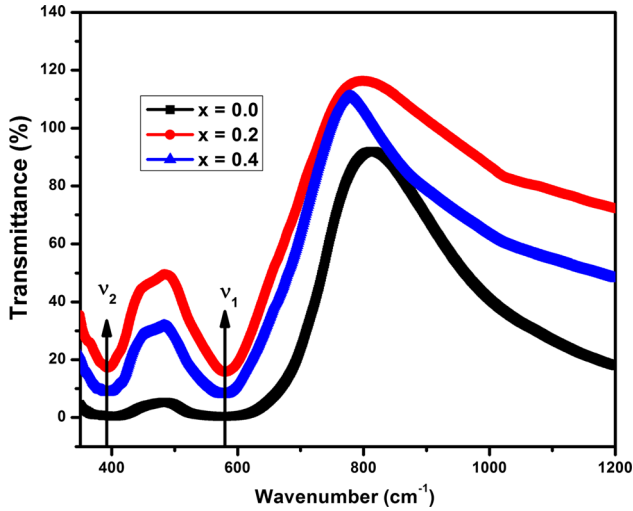
Fig. 6. FT-IR spectra of $\text{Co}_{0.5}\text{Cu}_x\text{Zn}_{0.5-x}\text{Fe}_2\text{O}_4$ nanoferrites.

Table III. Tetrahedral (ν_1) and Octahedral (ν_2) absorption bands $\text{Co}_{0.5}\text{Cu}_x\text{Zn}_{0.5-x}\text{Fe}_2\text{O}_4$ nanoferrites

Concentration (x)	$\nu_1 \text{ cm}^{-1}$ A-site	$\nu_2 \text{ cm}^{-1}$ B-site
0.0	524.661	399.28
0.2	579.633	378.99
0.4	579.634	393.49

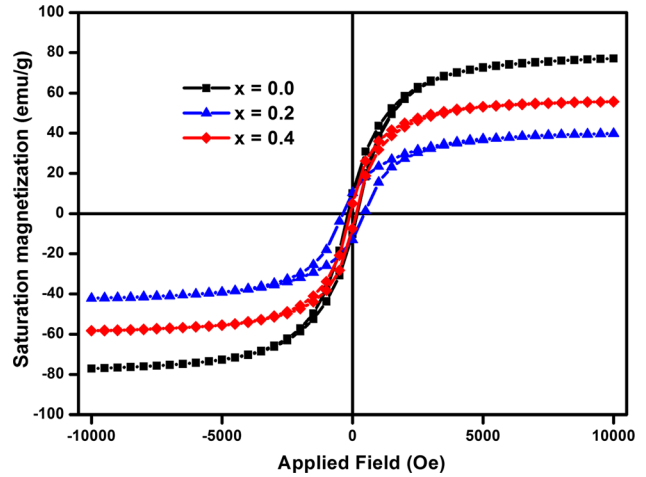
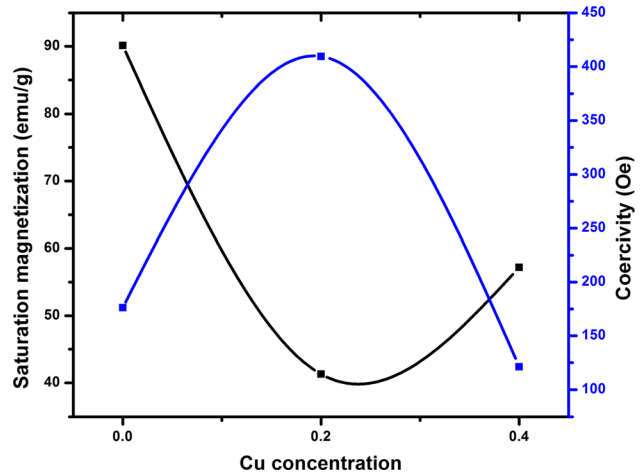
Bohr magneton (μ_{Bobs} and μ_{Bth}), and anisotropy constant (K) of $\text{Co}_{0.5}\text{Zn}_{0.5-x}\text{Cu}_x\text{Fe}_2\text{O}_4$ samples are listed in Table IV. The experimental Bohr Magnetone was calculated using the formula given as:⁴¹

$$\mu_B = \frac{M_{wt} \cdot M_s}{5585},$$

where M_{wt} is the molecular weight, and M_s is the saturation magnetization. In comparison with $\text{Co}_{0.5}\text{Zn}_{0.5}\text{Fe}_2\text{O}_4$ samples, Cu-doped samples exhibit lower Bohr magnetone values, which are dominant values of saturation magnetization.

DC Electrical Resistivity

The plot of DC resistivity ($\log \rho$) versus temperature ($10^3/T$) of prepared $\text{Co}_{0.5}\text{Cu}_x\text{Zn}_{0.5-x}\text{Fe}_2\text{O}_4$ ($x = 0.0, 0.2$ and 0.4) nanoferrites is shown in Fig. 9, which shows the inverse proportionality of resistivity with temperature. The graphs reveal the semi-conducting property of the synthesized ferrite nanoparticles.⁴⁰ Drift mobility of the charge carriers was increased by thermal excitations. The increase in temperature facilitates the hopping of electrons between Fe^{3+} and Fe^{2+} ions. The condition of sintering and the amount of hopping between Fe^{3+} and Fe^{2+} ions determine the number of such ion pairs.⁴² The DC electrical resistivity increases with

Fig. 7. Hysteresis loops for $\text{Co}_{0.5}\text{Cu}_x\text{Zn}_{0.5-x}\text{Fe}_2\text{O}_4$ nanoferrites.Fig. 8. Variation of saturation magnetization and coercivity of $\text{Co}_{0.5}\text{Cu}_x\text{Zn}_{0.5-x}\text{Fe}_2\text{O}_4$ nanoferrites.

increase in Cu^{2+} ions in $\text{Co}_{0.5}\text{Cu}_x\text{Zn}_{0.5-x}\text{Fe}_2\text{O}_4$ (from $x = 0.0, 0.2, 0.4$). The samples' activation energy can also be calculated from the slope change for all the materials under investigation. The mixed ferrites sintered in bulk have higher resistivity.⁴³ DC electrical resistivity depends on the grain size and the porosity and grain boundary area.

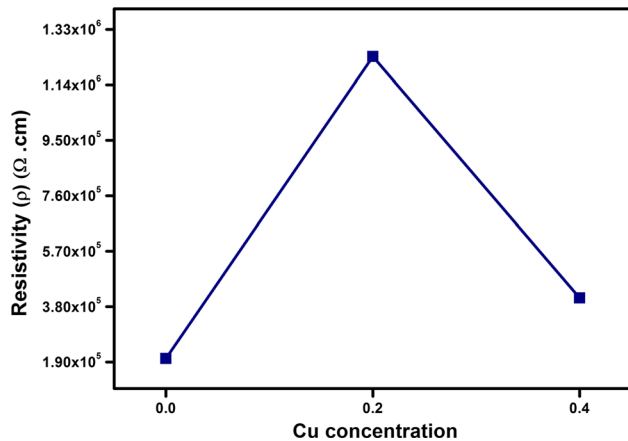
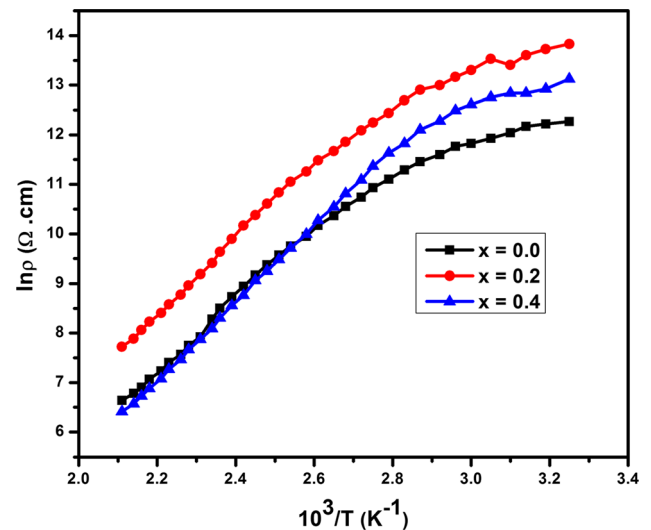
The resistivity can be determined for a given temperature by the relation,

$$\sigma_{ac} = \sigma_o \exp\left(-\frac{E_a}{k_B T}\right),$$

where ρ_o is the pre-exponential factor with dimensions of ($\Omega\text{-cm}$). The resistivity at T K, ΔE represents activation energy required for conduction, k_B indicates the Boltzmann constant and T is the absolute temperature.

Table IV. M_s , M_r , H_c , μ_{Bobs} , μ_{Bth} , and K of $Co_{0.5}Cu_xZn_{0.5-x}Fe_2O_4$ samples

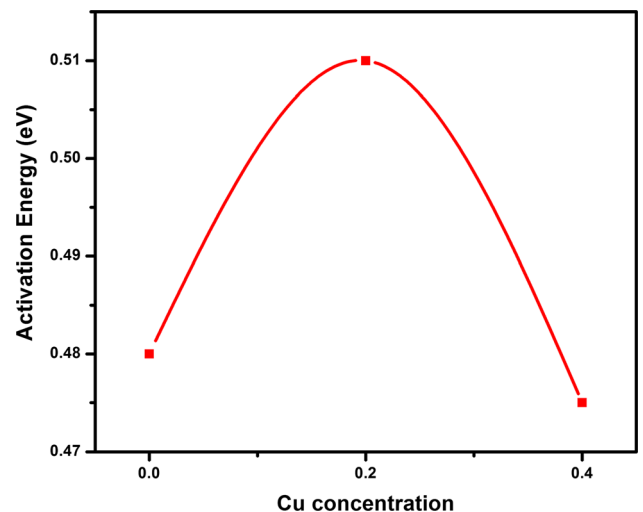
Concentration (x)	M_s (emu/g)	M_r (emu/g)	H_c (Oe)	μ_{Bobs}	μ_{Bth}	$K \times 10^4$ (erg/Oe)	$R=M_r/M_s$
0.0	90.13	11.23	176.24	3.81	6.35	1.63	0.129
0.2	41.3	11.5	409.5	1.72	5.51	1.73	0.288
0.4	57.2	6.4	121.21	2.38	5.15	0.76	0.13

Fig. 9. DC resistivity versus temperature of $Co_{0.5}Cu_xZn_{0.5-x}Fe_2O_4$ nanoferrites.Fig. 10. Variation of room temperature DC resistivity of $Co_{0.5}Cu_xZn_{0.5-x}Fe_2O_4$ nanoferrites.

The nature of the Cu concentration graphs with resistivity and activation energies is similar, as shown in Figs. 10 and 11, respectively. In the figures, the resistivity and activation energy first rises to a concentration of $x = 0.2$ and then decreases. This is due to the semiconducting gap present in the ferrites and super-exchange of cations at the two sites by the hopping process.⁴⁴

CONCLUSIONS

Sol-gel auto-combustion was used to prepare a series of Cu-substituted Co–Zn nanoferrite samples $Co_{0.5}Cu_xZn_{0.5-x}Fe_2O_4$ ($x = 0.0, 0.2$ and 0.4). XRD patterns show their crystalline nature. The Cu substituted powders were sintered at 1050°C for 3 hrs, giving a spinel cubic structure with a single phase. The reduced size of the resultant crystallite caused a significant effect on the structural and magnetic properties of the samples synthesized. With an irregular shape and non-uniform distribution in the microstructures' size, the grains and porosities were depicted in the FESEM images. FTIR spectroscopy's absorption band showed the cation vibrations of the mixed ferrites as their characteristic properties. The octahedral absorption band shifted towards the lower wavenumber side because of ionic radii reduction, resulting in bond length reduction and reduced wavenumber or increment in frequency. According to the AB–BA

Fig. 11. Variation of activation energy of $Co_{0.5}Cu_xZn_{0.5-x}Fe_2O_4$ nanoferrites

exchange interaction effect, the tetrahedral site somehow decreased the total magnetization of the samples. In a semi-disordered system like Co–Zn ferrite, a sudden tilting or overturning effect (canting) in magnetic moments decreases the

magnetization. Here, the value of coercivity was found to be maximum at $x=0.2$. The samples' DC electrical resistivity showed semiconducting behavior and the value of resistivity was increased with the dopant concentration, which is desirable for high-frequency devices. The tuned values of magnetic and DC resistivities obtained suggest the promising nature of the synthesized materials for technological applications.

ACKNOWLEDGEMENT

Author K M Batoo is thankful to Scientific Research's Deanship at King Saud University for financial support through the project Code (RG-1437-030).

CONFLICT OF INTEREST

The authors declare that they have no conflict of interest.

REFERENCES

1. T. Roman, R.L. Asavei, N.E. Karkalos, C. Roman, C. Virlan, N. Cimpoesu, B. Istrate, M. Zaharia, A.P. Markopoulos, K. Kordatos, S. Stanciu, and A. Pui, T. Roman, R.L. Asavei, N.E. Karkalos, C. Roman, C. Virlan, N. Cimpoesu, B. Istrate, M. Zaharia, A.P. Markopoulos, K. Kordatos, S. Stanciu, and A. Pui, *Int. J. Appl. Ceram. Technol.*, 2019, **16**, p 693.
2. C. Virlan, R.G. Ciocarlan, T. Roman, D. Gherca, N. Cornei, and A. Pui, C. Virlan, R.G. Ciocarlan, T. Roman, D. Gherca, N. Cornei, and A. Pui, *Acta Chem. Iasi.*, 2013, **21**, p 19.
3. E. Myrovali, N. Maniotis, A. Makridis, A. Terzopoulou, V. Ntomprougkidis, K. Simeonidis, D. Sakellari, O. Kalogirou, T. Samaras, R. Salikhov, M. Spasova, M. Farle, U. Wiedwald, and M. Angelakeris, E. Myrovali, N. Maniotis, A. Makridis, A. Terzopoulou, V. Ntomprougkidis, K. Simeonidis, D. Sakellari, O. Kalogirou, T. Samaras, R. Salikhov, M. Spasova, M. Farle, U. Wiedwald, and M. Angelakeris, *Sci. Rep.*, 2016, **6**, p 1.
4. L. Stanciu, Y.H. Won, M. Ganesana, and S. Andreescu, L. Stanciu, Y.H. Won, M. Ganesana, and S. Andreescu, *Sensors*, 2009, **9**, p 2976.
5. B. Sahoo, K.S.P. Devi, S. Dutta, T.K. Maiti, P. Pramanik, and D. Dhara, B. Sahoo, K.S.P. Devi, S. Dutta, T.K. Maiti, P. Pramanik, and D. Dhara, *J. Colloid Interface Sci.*, 2014, **431**, p 31.
6. A. Singh, S. Pathak, P. Kumar, P. Sharma, A. Rath, G.A. Basheed, K.K. Maurya, and R.P. Pant, A. Singh, S. Pathak, P. Kumar, P. Sharma, A. Rath, G.A. Basheed, K.K. Maurya, and R.P. Pant, *J. Magn. Magn. Mater.*, 2020, **493**, p 165737.
7. P.H. Nam, N.X. Phuc, D.K. Tung, V.Q. Nguyen, N.H. Nam, D.H. Manh, and P.T. Phong, P.H. Nam, N.X. Phuc, D.K. Tung, V.Q. Nguyen, N.H. Nam, D.H. Manh, and P.T. Phong, *Physica B Condens. Matter.*, 2020, **591**, p 412246.
8. V. Constantin, T. Florin, and P. Aurel, V. Constantin, T. Florin, and P. Aurel, *Int. J. Appl. Ceram. Technol.*, 2017, **14**, p 1174.
9. A. Ramakrishna, N. Murali, T.W. Mammo, K. Samatha, and V. Veeraiah, A. Ramakrishna, N. Murali, T.W. Mammo, K. Samatha, and V. Veeraiah, *Physica B Condens Matter*, 2018, **534**, p 134.
10. D. Gherca, A. Pui, V. Nica, O. Caltun, and N. Cornei, D. Gherca, A. Pui, V. Nica, O. Caltun, and N. Cornei, *Ceram. Int.*, 2014, **40**, p 9599.
11. A.I. Popov, Z.V. Gareeva, F.A. Mazhitova, and R.A. Doroshenko, A.I. Popov, Z.V. Gareeva, F.A. Mazhitova, and R.A. Doroshenko, *J. Magn. Magn. Mater.*, 2018, **461**, p 128.
12. N. Sangeneni, K.M. Taddei, N. Bhat, and S.A. Shivashankar, N. Sangeneni, K.M. Taddei, N. Bhat, and S.A. Shivashankar, *J. Magn. Magn. Mater.*, 2018, **465**, p 590.
13. S. Lalwani, R.B. Marichi, M. Mishra, G. Gupta, G. Singh, and R.K. Sharma, S. Lalwani, R.B. Marichi, M. Mishra, G. Gupta, G. Singh, and R.K. Sharma, *Electrochim. Acta.*, 2018, **283**, p 708.
14. L. Andjelkovic, M. Suljagic, M. Lakic, D. Jeremic, P. Vulic, and A.S. Nikolic, L. Andjelkovic, M. Suljagic, M. Lakic, D. Jeremic, P. Vulic, and A.S. Nikolic, *Ceram. Int.*, 2018, **44**, p 14163.
15. R.G. Ciocarlan, A. Pui, D. Gherca, C. Virlan, M. Dobromir, V. Nica, M.L. Craus, I.N. Gostin, O. Caltun, R. Hempelman, and P. Cool, R.G. Ciocarlan, A. Pui, D. Gherca, C. Virlan, M. Dobromir, V. Nica, M.L. Craus, I.N. Gostin, O. Caltun, R. Hempelman, and P. Cool, *Mater. Res. Bull.*, 2016, **81**, p 63.
16. G. Rekha, R. Tholkappiyar, K. Vishista, and F. Hamed, G. Rekha, R. Tholkappiyar, K. Vishista, and F. Hamed, *Appl. Surf. Sci.*, 2016, **385**, p 171.
17. P. Samoila, L. Sacarescu, A.I. Borhan, D. Timpu, M. Grigoras, N. Lupu, M. Zaltariov, and V. Harabagiu, P. Samoila, L. Sacarescu, A.I. Borhan, D. Timpu, M. Grigoras, N. Lupu, M. Zaltariov, and V. Harabagiu, *J. Magn. Magn. Mater.*, 2015, **378**, p 92.
18. H.M. Zhang, Z. Wang, J.J. Pei, and Y. Gao, H.M. Zhang, Z. Wang, J.J. Pei, and Y. Gao, *J. Sol. Gel Sci. Technol.*, 2019, **90**, p 404.
19. C. Virlan, G. Bulai, O.F. Caltun, R. Hempelmann, and A. Pui, C. Virlan, G. Bulai, O.F. Caltun, R. Hempelmann, and A. Pui, *Ceram. Int.*, 2016, **42**, p 11958.
20. S. Qamara, M.N. Akhtar, K.M. Batoo, and E.H. Raslan, S. Qamara, M.N. Akhtar, K.M. Batoo, and E.H. Raslan, *Ceram Int*, 2020, **46**, p 14481.
21. M.N. Akhtar, M. Babar, S. Qamar, Z. ur Rehman, and M.A. Khan, M.N. Akhtar, M. Babar, S. Qamar, Z. ur Rehman, and M.A. Khan, *Ceram Int*, 2019, **45**, p 10187.
22. A. Ramakrishna, N. Murali, S.J. Margarete, T.W. Mammo, N.K. Joythi, B. Sailaja, C.C.S. Kumari, K. Samatha, and V. Veeraiah, A. Ramakrishna, N. Murali, S.J. Margarete, T.W. Mammo, N.K. Joythi, B. Sailaja, C.C.S. Kumari, K. Samatha, and V. Veeraiah, *Adv Powder Technol*, 2018, **29**, p 2601.
23. G. Raju, N. Murali, M.S.N.A. Prasad, B. Suresh, D.A. Babu, M.G. Kiran, A. Ramakrishna, M.T. Wegayehu, and B.K. Babu, G. Raju, N. Murali, M.S.N.A. Prasad, B. Suresh, D.A. Babu, M.G. Kiran, A. Ramakrishna, M.T. Wegayehu, and B.K. Babu, *Mater. Sci. Energy Technol.*, 2019, **2**, p 78.
24. D.L. Navgare, V.B. Kawade, U.B. Tumberphale, S.S. Jadhav, R.S. Mane, and S.K. Gore, D.L. Navgare, V.B. Kawade, U.B. Tumberphale, S.S. Jadhav, R.S. Mane, and S.K. Gore, *J. Sol-Gel Sci. Technol.*, 2020, **93**, p 633.
25. T.W. Mammo, C.V. Kumari, S.J. Margarete, A. Ramakrishna, R. Vemuri, Y.B. Shankar Rao, K.L.V. Prasad, Y. Ramakrishna, and N. Murali, T.W. Mammo, C.V. Kumari, S.J. Margarete, A. Ramakrishna, R. Vemuri, Y.B. Shankar Rao, K.L.V. Prasad, Y. Ramakrishna, and N. Murali, *Phys. B Condens. Matter*, 2020, **581**, p 411769.
26. A.B. Mugutkar, S.K. Gore, R.S. Mane, K.M. Batoo, S.F. Adil, and S.S. Jadhav, A.B. Mugutkar, S.K. Gore, R.S. Mane, K.M. Batoo, S.F. Adil, and S.S. Jadhav, *Ceram. Int.*, 2018, **44**, p 21675.
27. M.A. Almessiere, M.A. Almessiere, *J. Rare Earth.*, 2019, **37**, p 1108.
28. A. Ramakrishna, N. Murali, S.J. Margarete, K. Samatha, and V. Veeraiah, A. Ramakrishna, N. Murali, S.J. Margarete, K. Samatha, and V. Veeraiah, *Phys. B Condens. Matter.*, 2018, **530**, p 251.
29. D.R. Mane, D.D. Birajdar, S. Patil, S.E. Shirsath, and R.H. Kadam, D.R. Mane, D.D. Birajdar, S. Patil, S.E. Shirsath, and R.H. Kadam, *J. Sol-Gel Sci. Technol.*, 2011, **58**, p 70.
30. T.W. Mammo, N. Murali, Y.M. Sileshi, and T. Arunamani, T.W. Mammo, N. Murali, Y.M. Sileshi, and T. Arunamani, *Phys. B Condens. Matter*, 2018, **531**, p 164.

31. A.B. Mugutkar, S.K. Gore, R.S. Mane, S.M. Patange, S.S. Jadhav, S.F. Shaikh, A.M. Al-Enizi, A. Nafady, B.M. Thamer, and M. Ubaidullah, A.B. Mugutkar, S.K. Gore, R.S. Mane, S.M. Patange, S.S. Jadhav, S.F. Shaikh, A.M. Al-Enizi, A. Nafady, B.M. Thamer, and M. Ubaidullah, *J. Alloys Compd.*, 2020, **844**, p 156178.
32. B.K. Labde, M.C. Sable, and N.R. Shamkuwar, B.K. Labde, M.C. Sable, and N.R. Shamkuwar, *Mater. Lett.*, 2003, **57**, p 1651.
33. N.H. Kumar, G. Aravind, D. Ravinder, T. Somaiah, and B.R. Reddy, N.H. Kumar, G. Aravind, D. Ravinder, T. Somaiah, and B.R. Reddy, *Int. J. Eng. Res. Appl.*, 2014, **4**, p 137.
34. M. AsifIqbal, M. Islam, I. Ali, M.A. Khan, S.M. Ramay, M.H. Khan, and M.K. Mehmood, M. AsifIqbal, M. Islam, I. Ali, M.A. Khan, S.M. Ramay, M.H. Khan, and M.K. Mehmood, *J. Alloy. Comp.*, 2017, **692**, p 322.
35. Y. Li, R. Liu, Z. Zhang, and C. Xiong, Y. Li, R. Liu, Z. Zhang, and C. Xiong, *Mater. Chem. Phys.*, 2000, **64**, p 256.
36. A. Monshi, M.R. Foroughi, and M.R. Monshi, A. Monshi, M.R. Foroughi, and M.R. Monshi, *World J. Nano Sci. Eng.*, 2012, **2**, p 154.
37. S. Morup, E. Brok, and C. Frandsen, S. Morup, E. Brok, and C. Frandsen, *J. Nanomater.*, 2013, **2013**, p 720629.
38. A.H.E. Foulani, A. Aamouche, F. Mohseni, J.S. Amaral, D.M. Tobaldi, and R.C. Pullar, A.H.E. Foulani, A. Aamouche, F. Mohseni, J.S. Amaral, D.M. Tobaldi, and R.C. Pullar, *J. Alloys Compd.*, 2019, **774**, p 1250.
39. A. Samokhralov, and A.G. Rustmov, A. Samokhralov, and A.G. Rustmov, *Sov. Phys. Solid State.*, 1965, **7**, p 961.
40. S.S. Abbas, I.H. Gul, S. Ameer, and M. Anees, S.S. Abbas, I.H. Gul, S. Ameer, and M. Anees, *Electron. Mater. Lett.*, 2015, **11**, p 100.
41. B.B.V.S. Vara. Prasad, K.V. Ramesh, and A. Sinivas, B.B.V.S. Vara. Prasad, K.V. Ramesh, and A. Sinivas, *Mater. Sci.Poland*, 2019, **37**, p 39.
42. B. Shinde, B. Shinde, *Int. J. Res. Eng. Appl. Sci.*, 2016, **6**, p 75.
43. S.A. Mazen, and N.I. Abu-Elsaad, S.A. Mazen, and N.I. Abu-Elsaad, *Appl. Nanosci.*, 2015, **5**, p 105.
44. D.S. Kumar, and K.C. Mouli, D.S. Kumar, and K.C. Mouli, *Int. J. Nanotechnol. Appl.*, 2010, **4**, p 51.

Publisher's Note Springer Nature remains neutral with regard to jurisdictional claims in published maps and institutional affiliations.